Published in final edited form as:
Invest Ophthalmol Vis Sci. 2008 June ; 49(6): 2661–2667. doi:10.1167/iovs.07-0501.

Imaging Polarimetry in Age-Related Macular Degeneration

Masahiro Miura[1,2,3], **Masahiro Yamanari**[1,3], **Takuya Iwasaki**[1,2], **Ann E. Elsner**[4], **Shuichi Makita**[1,3], **Toyohiko Yatagai**[5], and **Yoshiaki Yasuno**[1,3]

[1]Computational Optics and Ophthalmology Group, Tokyo Medical University, Tokyo, Japan

[2]Department of Ophthalmology, Tokyo Medical University, Tokyo, Japan

[3]Computational Optics Group, University of Tsukuba, Tsukuba, Japan

[4]School of Optometry, Indiana University, Bloomington, Indiana

[5]Institute of Applied Physics, University of Tsukuba, Tsukuba, Japan

Abstract

PURPOSE—To evaluate the birefringence properties of eyes with age-related macular degeneration (AMD). To compare the information from two techniques—scanning laser polarimetry (GDx) and polarization-sensitive spectral-domain optical coherence tomography (OCT)—and investigate how they complement each other.

METHODS—The authors prospectively examined the eyes of two healthy subjects and 13 patients with exudative AMD. Using scanning laser polarimetry, they computed phase-retardation maps, average reflectance images, and depolarized light images. To obtain polarimetry information with improved axial resolution, they developed a fiber-based, polarization-sensitive, spectral-domain OCT system and measured the phase retardation associated with birefringence in the same eyes.

RESULTS—Both GDx and polarization-sensitive spectral-domain optical coherence tomography detected abnormal birefringence at the locus of exudative lesions. Polarization-sensitive, spectral-domain OCT showed that in the old lesions with fibrosis, phase-retardation values were significantly larger than in the new lesions ($P = 0.020$). Increased scattered light and altered polarization scramble were associated with portions of the lesions.

CONCLUSIONS—GDx and polarization-sensitive spectral-domain OCT are complementary in probing birefringence properties in exudative AMD. Polarimetry findings in exudative AMD emphasized different features and were related to the progression of the disease, potentially providing a noninvasive tool for microstructure in exudative AMD.

Age-related macular degeneration (AMD) is a major cause of severe visual loss among older people in developed countries.1 In AMD, the severe loss of central vision is often attributed to exudative lesions. Accurate investigation of exudative lesions is crucial for accurate evaluation and treatment of exudative AMD.

Polarimetry techniques have been developed to emphasize selectively the different layers of the retina. The most typical polarimetry technique used in ophthalmology is scanning laser

Corresponding author: Masahiro Miura, Department of Ophthalmology, Tokyo Medical University, Kasumigaura Hospital, 3-20-1 Chuo, Ami, Inashiki, Ibaraki 3000395, Japan; m-miura@tokyo-med.ac.jp.

Disclosure: **M. Miura**, None; **M. Yamanari**, None; **T. Iwasaki**, None; **A.E. Elsner**, None; **S. Makita**, None; **T. Yatagai**, None; **Y. Yasuno**, None

polarimetry for glaucoma diagnosis.2,3 In the original conceptualization, the retardation of the retinal nerve fiber layer is estimated using the light returning from the ocular fundus.3,4 More recently, customized software to analyze data from scanning laser polarimetry was developed to investigate the polarization properties of macular disease.5,6 Multiply scattered light, which helps visualize the retinal pigment epithelial (RPE) layer and deep retinal lesions, was emphasized by detecting depolarized light and rejecting light that retains polarization.5–11 Phase-retardation maps were used to detect abnormal fibrotic changes in the retina.6 The borders of well-defined choroidal neovascular membrane (CNV) were clearly defined in the depolarized light image.6 Thus, scanning laser polarimetry has some potentiality to evaluate the macular disease. However, it does not provide depth-resolved information about the polarization properties of the retina. Therefore, the depth of the origin of the polarization change has not yet been demonstrated.

Optical coherence tomography (OCT) is a widely used imaging tool in ophthalmology,12 especially for retinal disease accompanied by morphologic changes, including AMD. Depth-resolved information about polarization has been obtained using polarization-sensitive optical coherence tomography (PS-OCT).13,14 Birefringence of the nerve fiber layer15 and polarization scramble at the retinal pigment epithelium16 were measured with time-domain PS-OCT, but three-dimensional measurements were limited because of the scanning speeds of these systems. Recently, dramatic advances in OCT technology17,18 have facilitated improvements in three-dimensional PS-OCT measurements. PS spectral-domain OCT (PS-SD-OCT)19–22 allows the collection of three-dimensional retinal information about polarization properties.19 The combination of scanning laser polarimetry and PS-SD-OCT offers a variety of possibilities for diagnosis. For instance, using the en face image of PS-SD-OCT, a direct comparison between scanning laser polarimetry and PS-SD-OCT is possible. Further, the origin of polarization changes in scanning laser polarimetry images can be detected and quantified with PS-SD-OCT. Structures seen in the scattered light images can be further probed in depth with PS-SD-OCT to determine the spatial relation of highly reflective structures or increased birefringence seen in PS-SD-OCT to a focal increase in scattered light in scanning laser polarimetry. Therefore, in this study, we compared scanning laser polarimetry images and PS-SD-OCT images of the same eyes to evaluate the birefringence properties of retinas with exudative AMD.

METHODS

Scanning Laser Polarimetry

We used data from a commercially available ellipsometer (GDx Nerve Fiber Analyzer: Laser Diagnostic Technologies, San Diego, CA) for scanning laser polarimetry. This system is a confocal scanning laser ophthalmoscope that analyzes the effect of the traversal of light through the eye on the polarization state of the light. Linearly polarized light at 780 nm scans the retina in a raster pattern, with a measurement area of 15° × 15° visual angle. The returning light is separated into two beams by a polarizing beam splitter and travels to the uncrossed polarized detector and the crossed detector. Acquisition time is 0.7 second for an image series.

In this study, we used a scanning laser polarimeter with a fixed compensator that has a magnitude of 60 nm and a polarization axis of 15° nasally downward (single-pass retardance), which is uniform across the pupil plane. This fixed compensator usually cannot cancel the corneal birefringence, and GDx images showed the macular bowtie pattern that is expected because of the interaction of corneal and foveal birefringence. A later model of GDx (GDx-VCC; Carl Zeiss Meditec, Dublin, CA) has a variable corneal compensator to reduce the influence of corneal birefringence on the measurements of retinal nerve fiber layer birefringence, but we chose the GDx with the fixed compensator for two reasons. First,

for the appropriate operation of the variable corneal compensator, the Henle fiber layer should be intact.3 However, microstructures of Henle fiber might be disrupted in the presence of significant macular disease,11 and macular strategies for neutralization of corneal birefringence using GDx-VCC can fail.23 Therefore, there are no obvious advantages of the GDx-VCC over the GDx with fixed compensator for advanced cases of AMD.23 Second, the instrument is in the same state for all patients tested, with the compensator differing only between left and right eyes; therefore, individual calibrations are unnecessary. The disadvantage of using the GDx with fixed compensator is that the polarimeter images are not comparable between patients. However, the images were sufficient for comparison with our PS-SD-OCT images.

The details of our computation for polarimetry images have been described previously; we computed the phase-retardation map, the depolarized light image, and the average reflectance image.5,6 After correction for eye movements, the phase-retardation map was computed from the modulation of the light returning to the crossed detector. The depolarized light image was computed as the minimum value of light returning to the crossed detector for all input polarization angles. The average reflectance image was computed as the grand mean of the light returning to both detectors for all input polarization states. This image represented the average relative reflectance of the retina and was similar to that obtained with a typical confocal scanning laser ophthalmoscope with polarization-insensitive detectors.5

Intensities of the computed polarimetry images varied widely, and, as expected, the phase-retardation maps were too dark for subjective evaluation without further manipulation. For better visualization, the distribution of intensities in each image was adjusted as follows: minimum to maximum intensities in the images were converted to a grayscale that ranged from 0 to 255 grayscale units.

PS-SD-OCT

Detailed description of the prototype PS-SD-OCT system, built by the Computational Optic Group at the University of Tsukuba, has been published.20 The light source is a superluminescent diode with a central wavelength of 840 nm and bandwidth of 50 nm. The experimental axial resolution is 8.3 μm in the air and 6.0 μm in tissue. With this system, all the elements of the Jones matrix involving birefringence of the optical fiber, cornea, and retina are obtained. To compensate birefringence of the optical fiber and cornea, the Jones matrix is diagonalized using the signal at the retinal surface.24 Retinal phase retardation is calculated from this Jones matrix–based algorithm, and the phase-retardation map of the eye is visualized as a depth-resolved image displayed on the scale of the conventional cross-sectional OCT intensity image.

The approximate measurement area is 3.8 mm × 3.8 mm on retina, and a raster scanning protocol from inferior to superior with 1023 A-scans × 140 B-scans is used for all measurements of PS-SD-OCT. The scanning rate was 27,700 A scans per second, and the acquisition time for three-dimensional images was 5.5 seconds. Data points corresponding to intensities below a criterion threshold are excluded in the phase-retardation images. In these images, the hue represents the phase retardation ranging from 0° to 180°, and the brightness represents the intensity of the OCT signals. In PS-OCT, the reflected light from deeper regions always passes through the upper media and thus involves the cumulative effect of the birefringence. Hence, the phase retardation measured by PS-OCT is cumulative along the depth, and cumulative phase retardation increases with increasing depth because the polarization is set to 0 at the retinal surface. For quantitative evaluation, we calculated the mean cumulative phase-retardation value at the deepest portion of the region of interest. To compare recent with longstanding lesions, we compared the mean cumulative phase-

retardation values at the CNVs that occurred within 2 months before the test (patients 6–9) and phase-retardation values at the disciform scars (patients 10–13).

Subjects

All investigations were performed using a protocol that adheres to the tenets of the Declaration of Helsinki, and it was approved by the Institutional Review Boards of the University of Tsukuba and Tokyo Medical University. For healthy subjects, two healthy Japanese volunteers (2 males; 46 and 26 years of age) without detectable ocular disease were selected. To evaluate exudative AMD, we prospectively examined 13 eyes of 13 Japanese patients (10 males, 3 females; 51–82 years of age [mean age, 72.1 years]; Table 1). Of these patients, 5 had RPE detachment, 3 had early-stage exudative AMD with predominantly classic choroidal neovascular membrane (CNV), 1 had exudative AMD with RPE tear, 3 had end-stage of exudative AMD with disciform scar, and 1 had a recurrence of CNV after photodynamic therapy. All eyes had sufficiently clear media for obtaining good-quality scanning laser polarimetry images and PS-SD-OCT images.

RESULTS

Healthy Subjects

In the GDx images of the healthy subjects, images differing in polarization content emphasized different aspects of features (Fig. 1). The average reflectance images clearly showed the high reflections at the center of the vessels observed at the major retinal vessels, and this finding is typical of confocal images (Fig. 1A).7,10,25 Phase-retardation maps showed the macular bowtie pattern that was expected because of the interaction of corneal and foveal birefringence, and there was a systematic radial change in birefringence (Fig. 1B). Superficial features, such as reflections at the center of the retinal vessels, were significantly reduced in the depolarized light images (Fig. 1C).7,10

The en face projection images generated from the three-dimensional intensity OCT data showed a clear retinal vascular pattern (Fig. 1D) and enabled precise registration of PS-SD-OCT data with images from scanning laser polarimetry. In the intensity images of B-scan PS-SD-OCT, all retinal layers typical in high-resolution OCT26–28 could be observed (Fig. 1E). In the cumulative phase-retardation images of the B-scan PS-SD-OCT, hue and brightness showed the phase retardation and intensity, respectively. In the normal retinas, the retardation image showed multiple layers of the brightness, which corresponded to the conventional OCT images of retina. However, hue of the retardation images in the normal retina was constant throughout the retina except the RPE layer, which means that the phase retardations were constant throughout these layers. Polarization scramble was observed at the RPE layer (Fig. 1F). The cumulative phase-retardation values at the intersection of inner and outer segments of photoreceptor in two healthy subjects were 15° and 16°, respectively.

Exudative AMD

For exudative AMD, we evaluated a range of pathologic changes, as described in Methods. In both GDx and PS-SD-OCT, polarimetry findings in exudative AMD emphasized different aspects of features and were related to the progression of the disease.

Five patients with RPE detachments were evaluated for this study (Table 1, Fig. 2). Color images showed RPE detachments and surrounding exudation (Fig. 2A). Average reflectance images clearly showed areas with RPE detachments as well, demarcated low-intensity areas that typically indicate the presence of fluid (Fig. 2B). In phase-retardation maps of the GDx, macular bowtie patterns were observed (Fig. 2C). The depolarized light images, similar to the average reflectance images, indicated RPE detachments surrounded by fluid, but there

was neither extensive pigment mottling of the retinal pigment epithelium nor evidence of retinal vascular anomalous complex activity indicating retinal damage (Fig. 2D). In the intensity images of OCT B-scan, the RPE detachments were clearly observed, and the microstructures of retinal layers from internal limiting membrane to retinal pigment epithelium were well preserved (Fig. 2E). In the B-scan cumulative phase-retardation images of PS-SD-OCT, polarization scramble at the RPE layers was clearly observed and implied that microstructures of retinal pigment epithelium were well preserved (Fig. 2F). This polarization scramble was also detected in the en face retardation image of PS-SD-OCT (Fig. 2G). In other retinal layers, retardations were low and constant throughout the retinas except in RPE layers, and there were no obvious abnormal birefringence at the RPE detachments in the PS-SD-OCT images.

We evaluated the three patients with early-stage exudative AMD with predominantly classic CNV (Table 1, Fig. 3). All patients noticed visual disturbances no more than 2 months before the test. Fluorescein angiograms demonstrated the areas of leakage (Fig. 3A). Average reflectance images of the GDx visualized the fluids in CNVs as low-intensity areas, with the surrounding exudates as bright features (Fig. 3B). Macular bowtie patterns in the phase-retardation maps of the GDx were observed; however, the contours were disrupted at the areas with exudation (Fig. 3C). The depolarized light images visualized CNVs as high-intensity areas surrounded by low-intensity areas (Fig. 3D). The intensity images of B-scan OCT showed CNVs as highly reflective lesions that elevated the overlying retinas, and the RPE layers were disrupted in a corresponding manner (Fig. 3E). CNVs had low birefringence in the cumulative phase-retardation images of B-scan PS-SD-OCT (Fig. 3F). This implied that the CNV contained only a small fibrotic change because increased amounts of proteins, such as collagen or fibrin, provide a strong birefringence signal well known in wound healing.29 Cumulative phase-retardation values at the CNVs were distributed from 20° to 42°. The RPE layers were disrupted to varying degrees, but the depths of the layers were fairly uniform, whereas the elevations of the overlying retinas varied greatly. Comparison of the left and right portions of the lesion and of the retinal pigment epithelium beneath the flatter portion compared with the more sloped portions of the lesion indicated that the changes shown for the deeper layers did not result solely from the signal being blocked by the different pathologic structures through the fluid associated with the lesion (Figs. 3E, 3F). These findings implied that the microstructure of retinal pigment epithelium was damaged to varying degrees beneath the lesion.

We evaluated a the eye of a patient with CNV and RPE tear (Table 1; Fig. 4). Indocyanine angiography clearly showed the RPE tear as a hypofluorescent area adjacent to CNV (Fig. 4A). The average reflectance images and the depolarized light image of GDx showed the RPE tear as a high-intensity area, consistent with previous near infrared imaging30 (Figs. 4B, 4D). In the depolarized light image, an area of CNV was shown as a spotted high-intensity area (Fig. 4D), and the CNV and RPE tear were surrounded by a low-intensity area. The macular bowtie pattern in the phase-retardation map of the GDx was disrupted in the area with exudation (Fig. 4C). The intensity image of the B-scan OCT showed the CNV as a highly reflective lesion, and this lesion had low birefringence in the PS-SD-OCT image (Figs. 4E, 4F). The cumulative phase-retardation value at the CNV was 31°. The RPE tear could be observed in the inferior-to-superior intensity image of B-scan OCT and was clearly demonstrated as a discontinuity of intensity and of polarization scramble in PS-SD-OCT images (Figs. 4G, 4H).

We evaluated three eyes at the end stage of exudative AMD with disciform scars (Table 1; Fig. 5). Color images showed the light-scattering properties of scars (Fig. 5A). Average reflectance images of the GDx showed the disciform scars as high-intensity areas demarcated with neighboring low-intensity areas (Fig. 5B). In the phase-retardation maps of

the GDx, abnormal strong birefringence at the disciform scars— but no obvious macular bowtie—was observed (Fig. 5C). The depolarized light images showed disciform scars as low-intensity areas that included smaller bright regions surrounded by pigment changes (Fig. 5D). In the intensity images of B-scan OCT, highly reflective layers were observed in deep retinal layers, and the RPE layers were hardly distinguishable (Fig. 5E). In the phase-retardation images of B-scan PS-SD-OCT, areas of abnormal birefringence were observed corresponding to these highly reflective layers, and polarization scramble at the RPE layer could not be detected (Fig. 5F). Cumulative phase-retardation values at the CNVs were distributed from 115° to 127°. In the cutaway volumes of phase-retardation images of PS-SD-OCT, there were sharp changes across the retinas that were not seen in normal eyes (Fig. 5G). Areas with abnormal birefringence corresponded to areas with disciform scars and areas with abnormal birefringence in GDx images.

In an eye with recurrence after photodynamic therapy, two distinctive exudative lesions were observed in the color fundus photograph (Table 1; Fig. 6A). One was a disciform scar and the other was a new exudative lesion, as demonstrated by fluorescein angiography (Fig. 6B). The polarization properties of these exudative lesions were completely different. The average reflectance image of GDx showed the disciform scar as high-intensity area and the new exudative lesion as a low-intensity area (Fig. 6C). In the phase-retardation map, the disciform scar had a clear-cut region of strong birefringence, and the new lesion showed only weak birefringence. No macular bowtie was present (Fig. 6D). In the depolarized light image, the margin of the new lesion could be detected, and a choroidal vessel could be visualized in the area with the disciform scar (Fig. 6E). In the intensity image of B-scan OCT, both lesions appeared as highly reflective areas and did not clearly distinguish the contents of two lesions (Fig. 6F). The phase-retardation image of the B-scan PS-SD-OCT clearly distinguished the contents of two lesions. The area with the disciform scar showed clearly abnormal birefringence, whereas the new exudative lesion showed only subtle birefringence differences from the surrounding retina (Fig. 6G). The cumulative phase-retardation value at the new CNV was 39°, but at the scar it was 137°. The polarization scramble at the RPE layer was difficult to detect. In the cutaway volume of phase-retardation images of PS-SD-OCT, again strong changes were found across the retina (Fig. 6H). The area with abnormal birefringence corresponded to the area with the disciform scar and the area with abnormal birefringence in the GDx image.

We compared mean cumulative phase retardation across patients with the lesions that occurred within 2 months in one group (patients 6–9) and the older disciform scars in another group (patients 10–12; Fig. 7). Retardation values at the disciform scars were significantly higher than CNVs ($P = 0.020$, Mann-Whitney U test; Fig. 8).

DISCUSSION

In this study, we compared GDx images and PS-SD-OCT images and evaluated polarization analysis as a noninvasive technique for the investigation of the stages of exudative AMD. In the polarization image of AMD, striking polarization changes were observed at the disciform scars in GDx images and PS-SD-OCT images. Areas of these polarization changes were consistent across the two systems. Retardation values at disciform scars were significantly higher than at recent CNVs. The polarization scramble at the RPE layer in PS-SD-OCT images was disrupted to various degrees, as expected, by the location and severity of the pathologic changes. The borders of well-defined CNV could be clearly detected in the depolarized light image.6

These polarimetry findings provide information about the microstructure of the retina. Variations in the molecular compositions of the lesion components and determination of

which tissues provide the strongest birefringence signal are two factors in polarization changes in light returning from the retinas of eyes with exudative AMD. Disciform scarring in exudative AMD contains an abnormal fibrotic change.31 These fibrotic changes are composed of proteins that demonstrate birefringent properties.14,29 In the early stage of exudative AMD, this fibrotic change is not prominent,31 and only a small birefringence change at the exudation could be observed. This polarimetry finding is useful in the evaluation of the microstructures at the highly reflective layer in OCT images, as shown in the patients with disciform scar with new exudative lesions (Fig. 6). The phase-retardation image of PS-SD-OCT could discriminate polarization properties of two lesions, whereas the intensity image of OCT could not discriminate the contents of two lesions (Fig. 6). PS-SD-OCT could provide useful information about the microstructure of exudative lesions that could not be provided by conventional intensity-based OCT. Polarimetry imaging also provides information about the integrity of the microstructure of the retina. Polarization scramble at the RPE layer in PS-SD-OCT implies that microstructures of the retinal pigment epithelium are well preserved16 and may be used as the optical signature of an intact retinal pigment epithelium, against which an RPE tear could be compared and thus detected. Polarimetry imaging provided additional information that could not be obtained with conventional en face imaging or OCT.

PS-SD-OCT has the potential to evaluate the polarization properties of macular disease. Three-dimensional information about intensity and polarization properties were obtained and provided en face information similar to that of GDx phase-retardance maps. However, PS-SD-OCT is still in the development stage and is not commercially available. Maintenance and operation are more complicated than commercialized OCT. The GDx is a commercially available system and has a long and continuing literature for clinical application in glaucoma2 and macular disease.5–11 A practical advantage of GDx over PS-SD-OCT is that the testing time of GDx (0.7 second) is shorter than that of PS-SD-OCT (5.5 seconds). The GDx is an effective system for easily obtaining the polarization state at the region of interest, and it provides information concerning multiply scattered light as well as birefringence. With PS-SD-OCT, the origin of the polarization change could be readily detected and could provide more information about polarization properties of retinal disease. A combination of GDx and PS-SD-OCT is an effective tool to understand the polarization properties of retinal disease.

Acknowledgments

The authors thank Christoph K. Hitzenberger for fruitful discussion.

Supported in part by Grant-in-Aid for Scientific Research 15760026 from the Japan Society for the Promotion of Science, Japan Science and Technology Agency; the Special Research Project of Nanoscience at University of Tsukuba; and National Institutes of Health/National Eye Institute Grant EY007624 (AEE).

References

1. Klein R, Klein BE, Linton KL. Prevalence of age-related maculopathy: the Beaver Dam Eye Study. Ophthalmology. 1992; 99:933–943. [PubMed: 1630784]
2. Weinreb RN, Shakiba S, Zangwill L. Scanning laser polarimetry to measure the nerve fiber layer of normal and glaucomatous eyes. Am J Ophthalmol. 1995; 119:627–636. [PubMed: 7733188]
3. Zhou Q, Weinreb RN. Individualized compensation of anterior segment birefringence during scanning laser polarimetry. Invest Ophthalmol Vis Sci. 2002; 43:2221–2228. [PubMed: 12091420]
4. Dreher AW, Reiter K, Weinreb RN. Spatially resolved birefringence of the retinal nerve fiber layer. Appl Opt. 1992; 31:3730–3735. [PubMed: 20725346]
5. Burns SA, Elsner AE, Mellem-Kairala MB, Simmons RB. Improved contrast of subretinal structures using polarization analysis. Invest Ophthalmol Vis Sci. 2003; 44:4061–4068. [PubMed: 12939329]

6. Elsner AE, Weber A, Cheney MC, van Nasdale DA, Miura M. Imaging polarimetry in patients with neovascular age related macular degeneration. J Opt Soc Am A. 2007; 24:1468–1480.
7. Weber A, Cheney MC, Smithwick QYJ, Elsner AE. Polarimetric imaging and blood vessel quantification. Opt Express. 2004; 12:5178–5190. [PubMed: 19484075]
8. Mellem-Kairala MB, Elsner AE, Weber A, Simmons RB, Burns SA. Improved contrast of peripapillary hyperpigmentation using polarization analysis. Invest Ophthalmol Vis Sci. 2005; 46:1099–1106. [PubMed: 15728571]
9. Miura M, Elsner AE, Weber A, et al. Imaging polarimetry in central serous chorioretinopathy. Am J Ophthalmol. 2005; 140:1014–1019. [PubMed: 16376644]
10. Miura M, Elsner AE, Cheney MC, Usui M, Iwasaki T. Imaging polarimetry and retinal blood vessel quantification at the epiretinal membrane. J Opt Soc Am A. 2007; 24:1431–1437.
11. Weber A, Elsner AE, Miura M, Kompa S, Cheney MC. Relationship between foveal birefringence and visual acuity in neovascular age-related macular degeneration. Eye. 2007; 21:353–361. [PubMed: 16397620]
12. Huang D, Swanson E, Lin C, et al. Optical coherence tomography. Science. 1991; 254:1178–1181. [PubMed: 1957169]
13. Hee MR, Huang EA, Swanson EA, Fujimoto JG. Polarization-sensitive low-coherence reflectometer for birefringence characterization and ranging. J Opt Soc Am B. 1992; 9:903–908.
14. de Boer JF, Milner MJ, van Gemert JC, Nelson JS. Two-dimensional birefringence imaging in biological tissue. Opt Lett. 1997; 22:934–936. [PubMed: 18185711]
15. Cense B, Chen TC, Park BH, Pierce MC, de Boer JF. In vivo birefringence and thickness measurements of the human retinal nerve fiber layer using polarization-sensitive optical coherence tomography. J Biomed Opt. 2004; 9:121–125. [PubMed: 14715063]
16. Pircher M, Gotzinger E, Findl O, et al. Human macula investigated in vivo with polarization-sensitive optical coherence tomography. Invest Ophthalmol Vis Sci. 2006; 47:5487–5494. [PubMed: 17122140]
17. Wojtkowski M, Bajraszewski T, Targowski P, Kowalczyk A. Real-time in vivo imaging by high-speed spectral optical coherence tomography. Opt Lett. 2003; 28:1745–1747. [PubMed: 14514087]
18. Nassif NA, Cense B, Park BH, et al. In vivo high-resolution video-rate spectral-domain optical coherence tomography of the human retina and optic nerve. Opt Express. 2004; 12:367–376. [PubMed: 19474832]
19. Gotzinger E, Pircher M, Hitzenberger CK. High speed spectral domain polarization sensitive optical coherence tomography of the human retina. Opt Express. 2005; 13:10217–10229. [PubMed: 19503236]
20. Yamanari M, Makita S, Madjarova VD, Yatagai T, Yasuno Y. Fiber-based polarization-sensitive Fourier domain optical coherence tomography using B-scan-oriented polarization modulation method. Opt Express. 2006; 14:6502–6515. [PubMed: 19516828]
21. Yasuno Y, Makita S, Sutoh Y, Itoh M, Yatagai T. Birefringence imaging of human skin by polarization-sensitive spectral interferometric optical coherence tomography. Opt Lett. 2002; 27:1803–1805. [PubMed: 18033369]
22. Cense, B. Optical Coherence Tomography for Retinal Imaging (dissertation). Enschede, Netherlands: Twente University; 2005.
23. Bagga H, Greenfield DS, Knighton RW. Scanning laser polarimetry with variable corneal compensation: identification and correction for corneal birefringence in eyes with macular disease. Invest Ophthalmol Vis Sci. 2003; 44:1969–1976. [PubMed: 12714631]
24. Park BH, Pierce MC, Cense B, de Boer JF. Jones matrix analysis for a polarization-sensitive optical coherence tomography system using fiber-optic components. Opt Lett. 2004; 29:2512–2514. [PubMed: 15584278]
25. Bartsch DU, Freeman WR. Laser-tissue interaction and artifacts in confocal scanning laser ophthalmoscopy and tomography. Neurosci Biobehav Rev. 1993; 17:459–467. [PubMed: 8309654]
26. Cense B, Nassif NA, Chen T, et al. Ultrahigh-resolution high-speed retinal imaging using spectral-domain optical coherence tomography. Opt Express. 2004; 12:2435–2447. [PubMed: 19475080]

27. Drexler W, Morgner U, Ghanta RK, Kartner FX, Schuman JS, Fujimoto JG. Ultrahigh-resolution ophthalmic optical coherence tomography. Nat Med. 2001; 7:502–507. [PubMed: 11283681]

28. Wojtkowski M, Srinivasan V, Ko T, Fujimoto JG, Kowalczyk A, Duker J. Ultrahigh-resolution, high-speed, Fourier domain optical coherence tomography and methods for dispersion compensation. Opt Express. 2004; 12:2404–2422. [PubMed: 19475077]

29. Pierce MC, Strasswimmer J, Park BH, Cense B, de Boer JF. Advances in optical coherence tomography imaging for dermatology. J Invest Dermatol. 2004; 123:458–463. [PubMed: 15304083]

30. Elsner AE, Burns SA, Weiter J, Delori F. Infrared imaging of subretinal structures in the human ocular fundus. Vision Res. 1996; 36:191–205. [PubMed: 8746253]

31. Spencer, WH. Ophthalmic Pathology: An Atlas and Textbook. 3rd ed.. Philadelphia: WB Saunders; 1985. p. 926-982.

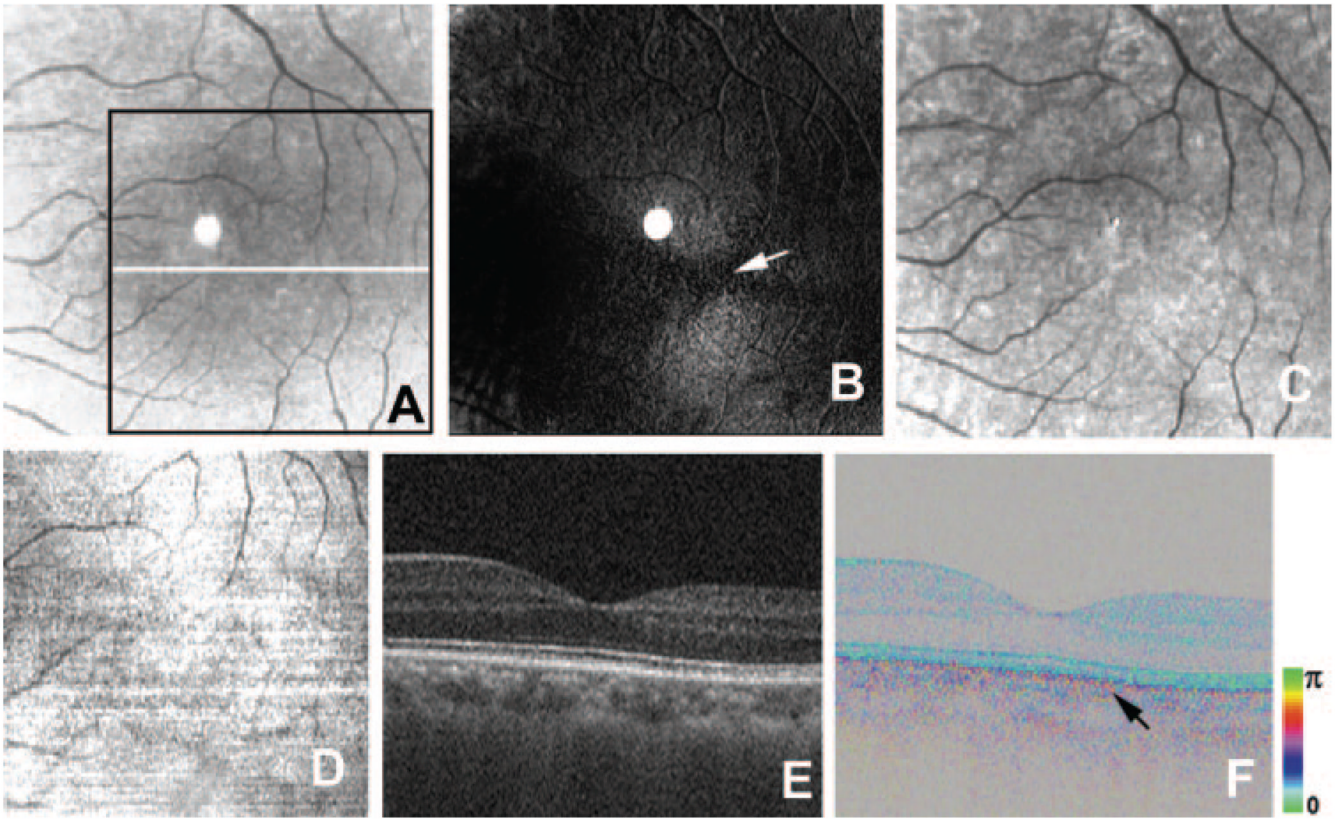

FIGURE 1.

Healthy left eye of a 46-year-old man. (**A**) Average reflectance image of GDx. *Black line*: area of PS-SD-OCT imaging in (**D**). *White line*: scanning line for the B-scan PS-SD-OCT images in (**E**, **F**). The *bright spot* in the center of the GDx image was an instrument artifact. (**B**) Phase-retardation map of GDx. *White arrow*: center of macular bowtie appearance. (**C**) Depolarized light image of GDx. (**D**) En face projection intensity image of PS-SD-OCT. (**E**) B-scan intensity image of PS-SD-OCT. (**F**) B-scan cumulative phase-retardation image. *Black arrow*: polarization scramble at the RPE layer.

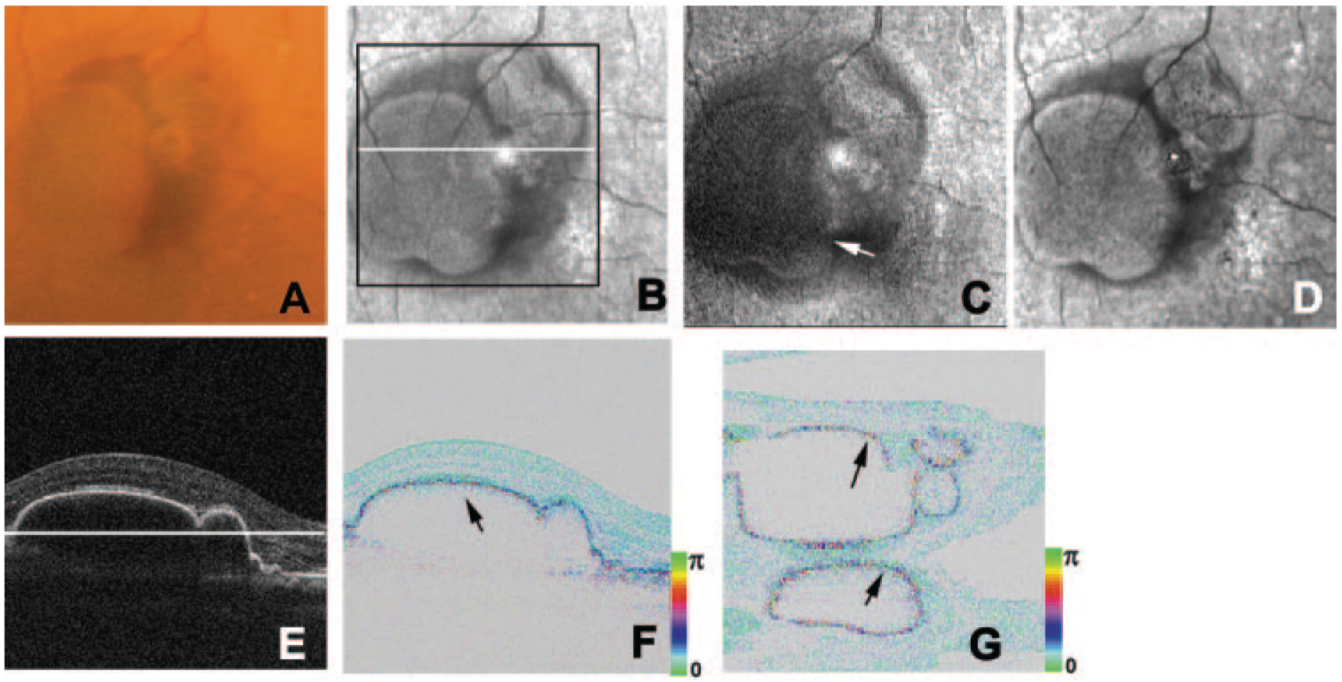

FIGURE 2.

Right eye of a 72-year-old woman with pigment epithelial detachment. (**A**) Color fundus photograph. (**B**) Average reflectance image of GDx. *Black line*: area of PS-SD-OCT imaging. *White line*: scanning line of PS-SD-OCT in (**E**, **F**). The *bright spot* in the center of the GDx image was an instrument artifact. (**C**) Phase-retardation map of GDx. *White arrow*: center of the macular bowtie. (**D**) Depolarized light image of GDx. (**E**) B-scan intensity image of PS-SD-OCT. *White line*: plane for en face image in Figure 3G. (**F**) B-scan cumulative phase-retardation image. *Black arrow*: polarization scramble at the RPE layer. (**G**) En face cumulative phase-retardation image. *Black arrows*; polarization scramble at the RPE layer.

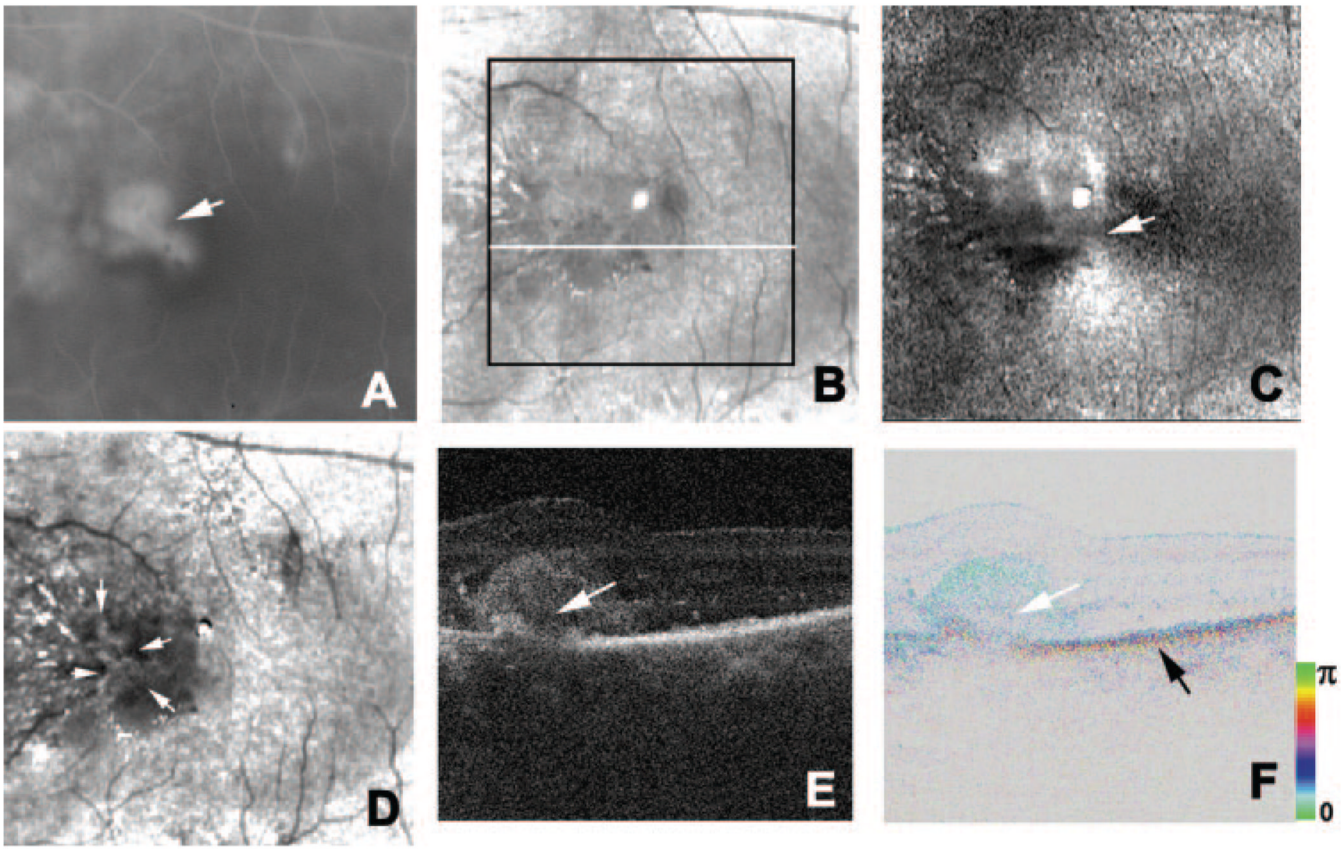

FIGURE 3.

Left eye of a 75-year-old man with early-stage exudative AMD with predominantly classic CNV. (**A**) Fluorescein angiography image. *White arrow*: CNV. (**B**) Average reflectance image of GDx. *Black line*: area of PS-SD-OCT imaging. *White line*: scanning line of PS-SD-OCT (**E**, **F**). A *bright spot* in the center of the GDx image was an instrument artifact. (**C**) Phase-retardation map of the GDx. *White arrow*: center of macular bowtie appearance. (**D**) Depolarized light image of GDx. *White arrows*: high-intensity area corresponding to the CNV. (**E**) B-scan intensity image of PS-SD-OCT. *White arrow*: highly reflective layer corresponding to the CNV. (**F**) B-scan cumulative phase-retardation image. *White arrow*: layer corresponding to the CNV. *Black arrow*: polarization scramble at the RPE layer.

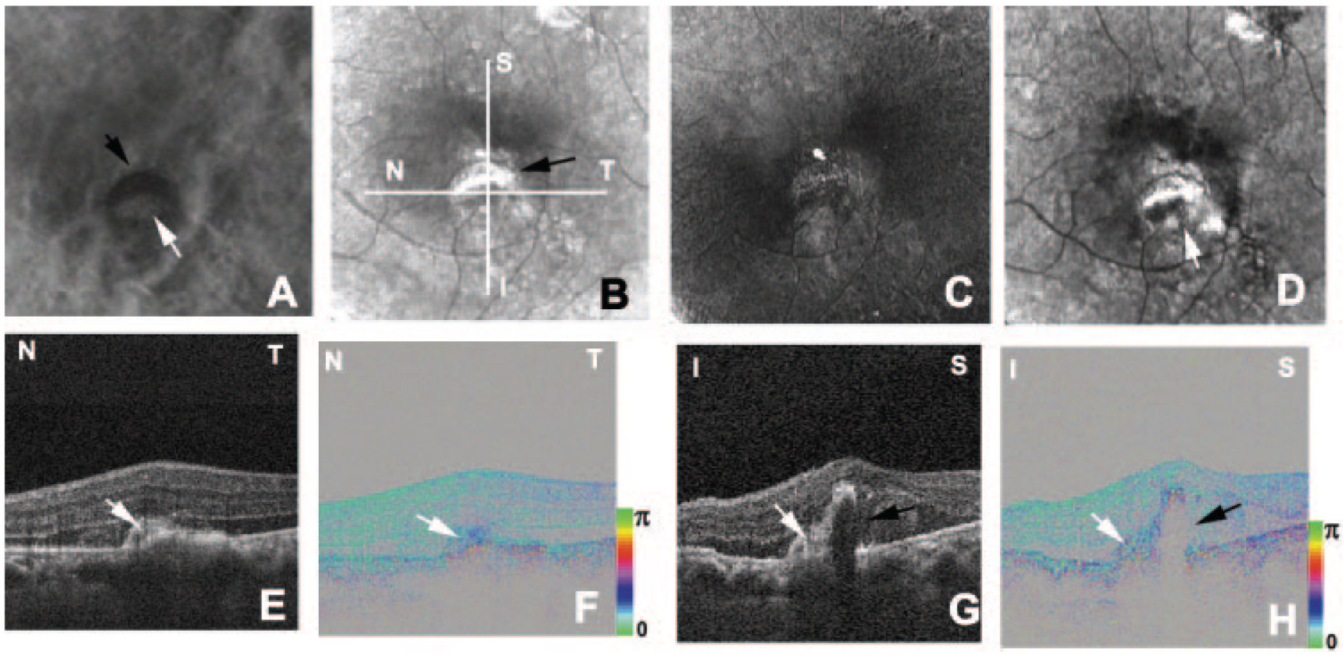

FIGURE 4.

Left eye of a 57-year-old man with exudative AMD and RPE tear. (**A**) Indocyanine green angiography image. *Black arrow*: RPE tear. *White arrow*: CNV. (**B**) Average reflectance image of GDx. *Black arrow*: RPE tear. *White lines*: scanning lines of PS-SD-OCT (**E–H**). A *bright spot* in the center of the GDx image was an instrument artifact. (**C**) Phase-retardation map of GDx. (**D**) Depolarized light image of GDx. *White arrow*: spotted high-intensity area corresponding to the CNV. (**E**) Horizontal B-scan intensity image of PS-SD-OCT. *White arrow*: highly reflective layer corresponding to the CNV. (**F**) Horizontal B-scan phase-retardation image of PS-SD-OCT. *White arrow*: CNV. (**G**) Vertical B-scan intensity image of PS-SD-OCT. *Black arrow*: RPE tear. *White arrow*: CNV. (**H**) Vertical B-scan phase-retardation image of PS-SD-OCT. *Black arrow*: RPE tear. *White arrow*: CNV.

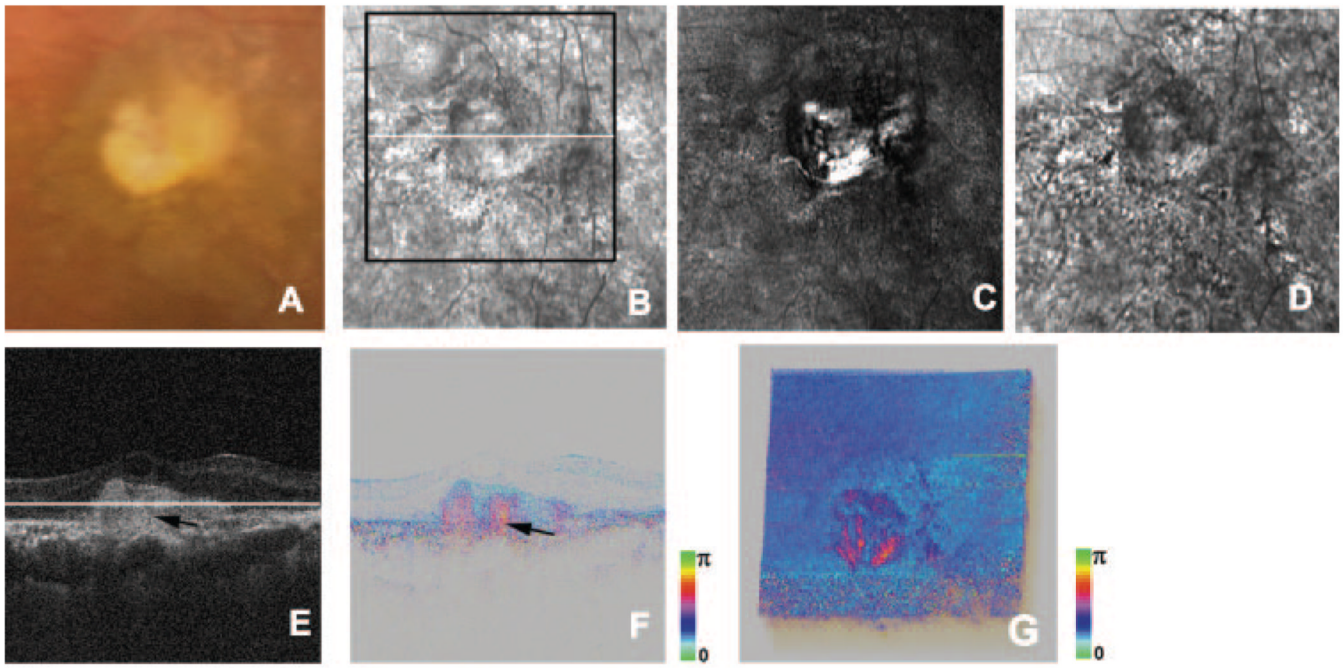

FIGURE 5.

Left eye of a 75-year-old man with late-stage exudative AMD with disciform scar. (**A**) Color fundus photograph. (**B**) Average reflectance image of GDx. *Black line*: area of PS-SD-OCT imaging. *White line*: scanning line of PS-SD-OCT (**E–G**). A *bright spot* in the center of the GDx image was an instrument artifact. (**C**) Phase-retardation map of GDx. (**D**) Depolarized light image of GDx. (**E**) B-scan intensity image of PS-SD-OCT. *White line*: plane for cutaway volume image in Figure 6G. (**F**) B-scan cumulative phase-retardation image. (**G**) Cutaway volume image of cumulative phase-retardation image.

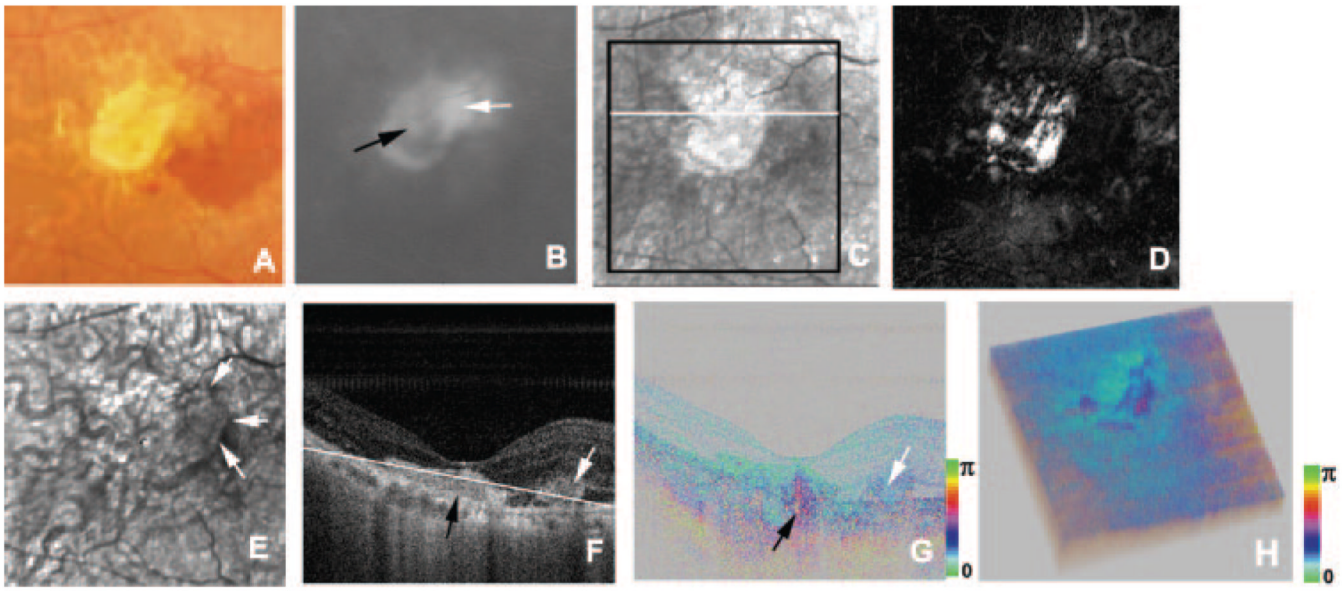

FIGURE 6.

Right eye of a 66-year-old man with a disciform scar and a new exudative lesion. (**A**) Color fundus photograph. (**B**) Fluorescein angiography image shows a new CNV (*white arrow*) adjacent to the disciform scar (*black arrow*). (**C**) Average reflectance image of GDx. *Black line*: area of PS-SD-OCT imaging. *White line*: scanning line of PS-SD-OCT (**F–H**). A *bright spot* in the center of the GDx image was an instrument artifact. (**D**) Phase-retardation map of GDx. (**E**) Depolarized light image of GDx. *White arrows*: new CNV. (**F**) B-scan intensity image of PS-SD-OCT. *White arrow*: new CNV. *Black arrow*: disciform scar. *White line*: plane for cutaway volume image (**H**). (**G**) B-scan cumulative phase-retardation image. *White arrow*: new CNV. *Black arrow*: disciform scar. (**H**) Cutaway volume image of cumulative phase-retardation image.

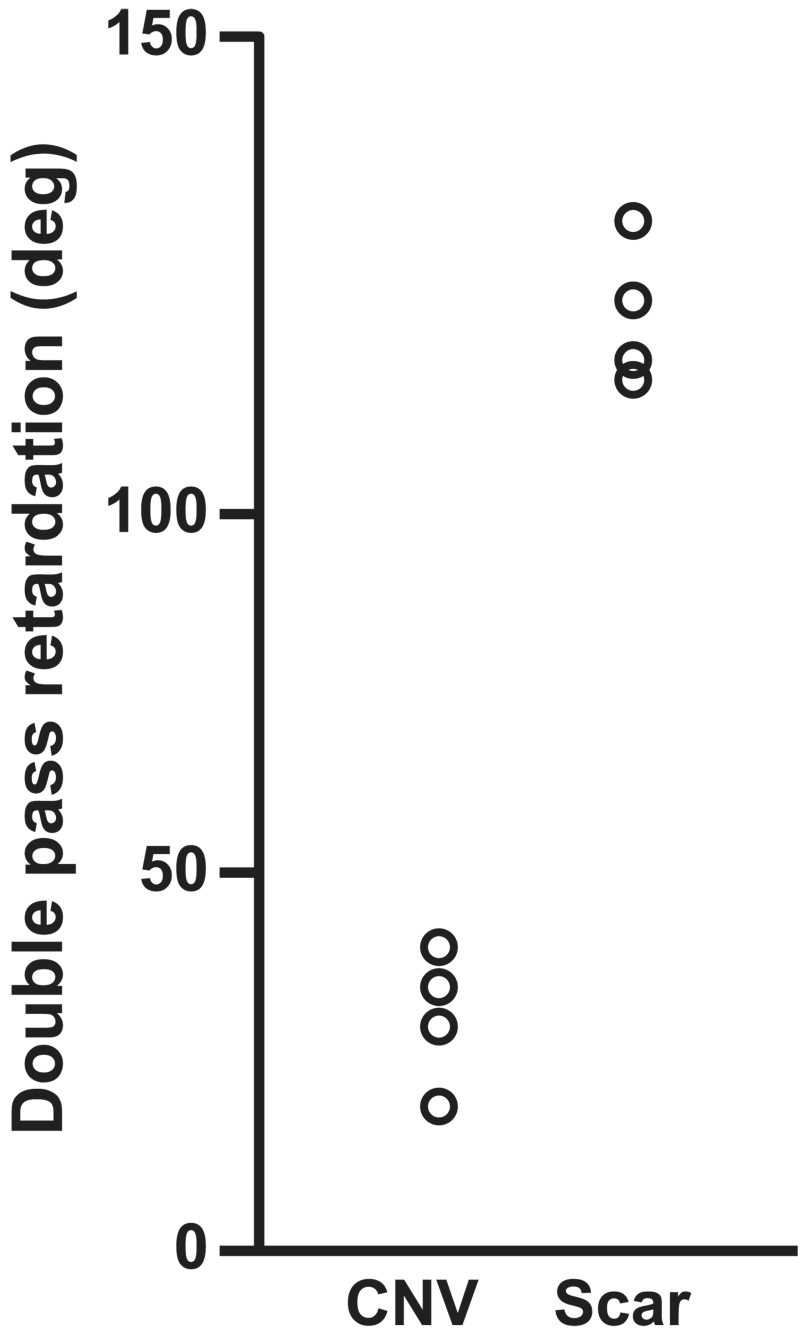

FIGURE 7.
Mean cumulative phase-retardation values at the CNVs that occurred within 2 months before the test and the values at the disciform scars.

TABLE 1

Clinical Characteristics in the Patients with Exudative AMD

Patient	Age (years)	Sex	Eye	Duration	VA	Exudative Lesion	Figure
1	72	F	R	1 wk	20/32	PED	2
2	51	M	L	1 y	20/100	PED	
3	81	F	L	3 mo	20/32	PED	
4	82	M	R	2 mo	20/50	PED	
5	81	M	R	2 y	20/400	PED	
6	75	M	L	1 mo	20/40	Early stage + predominantly classic CNV	3
7	71	M	L	2 mo	20/40	Early stage + predominantly classic CNV	
8	78	M	R	1 mo	20/40	Early stage + predominantly classic CNV	
9	57	M	L	2 mo	20/25	CNV + RPE tear	4
10	75	M	L	4 y	20/200	Disciform scar	5
11	74	M	R	2 y	20/200	Disciform scar	
12	81	F	R	5 y	20/400	Disciform scar	
13	66	M	R	5 y	20/200	Disciform scar with new CNV	6

VA, best-corrected visual acuity; PED, pigment epithelial detachment; RPE tear, retinal pigment epithelial tear.